



ELSEVIER

Contents lists available at SciVerse ScienceDirect

## International Journal of Heat and Mass Transfer

journal homepage: [www.elsevier.com/locate/ijhmt](http://www.elsevier.com/locate/ijhmt)

## Computational modeling and design of actively-cooled microvascular materials

Soheil Soghrati<sup>a,b</sup>, Piyush R. Thakre<sup>a</sup>, Scott R. White<sup>a,c</sup>, Nancy R. Sottos<sup>a,d</sup>, Philippe H. Geubelle<sup>a,c,\*</sup><sup>a</sup> Beckman Institute for Advanced Science and Technology, University of Illinois at Urbana-Champaign, 405 North Mathews Avenue, Urbana, IL 61801, USA<sup>b</sup> Department of Civil and Environmental Engineering, University of Illinois at Urbana-Champaign, 205 North Mathews Avenue, Urbana, IL 61801, USA<sup>c</sup> Department of Aerospace Engineering, University of Illinois at Urbana-Champaign, 104 South Wright Street, Urbana, IL 61801, USA<sup>d</sup> Department of Materials Science and Engineering, University of Illinois at Urbana-Champaign, 1304 West Green Street, Urbana, IL 61801, USA

## ARTICLE INFO

## Article history:

Received 24 November 2011

Received in revised form 9 May 2012

Accepted 15 May 2012

Available online 14 June 2012

## Keywords:

GFEM/XFEM

Convection–diffusion equation

Microvascular materials

Shape optimization

Biomimetic

Active cooling

Infrared imaging

## ABSTRACT

The computational modeling and design of an actively-cooled microvascular fin specimen is presented. The design study is based on three objective functions: (i) minimizing the maximum temperature in the thermally loaded fin, (ii) optimizing the flow efficiency of the embedded microchannel, and (iii) minimizing the void volume fraction of the microvascular material. A recently introduced Interface-enriched Generalized Finite Element Method (IGFEM) is employed to evaluate the temperature field in a 2D model of the specimen, allowing for the accurate and efficient capturing of the gradient discontinuity along the fluid/solid interface without the need of meshes that conform to the geometry of the problem. Finding the optimal shape of the embedded microchannel is thus accomplished with a single non-conforming mesh for all configurations. Prior to the optimization study, the IGFEM solver is validated through comparison with infrared measurements of the thermal response of an epoxy fin with a sinusoidal microchannel.

© 2012 Elsevier Ltd. All rights reserved.

## 1. Introduction

Modeled after circulatory systems found in many living organisms, microvascular materials with microchannels of diameters ranging from 10  $\mu\text{m}$  to 1 mm, embedded in polymeric matrices, have shown great promise in a variety of engineering applications such as autonomic healing and active cooling [1–3]. Recent advances in manufacturing techniques for microfluidic materials and devices [4,5] have extended the application of such systems to a broad field including autonomic materials [6], biotechnology [7,8], chemical reactors [9], and microelectromechanical systems (MEMS) [10–12]. In many of these applications, biomimicry has been used as an inspiration for the design of the microvascular system, while manufacturing constraints often play a key role in restricting the design space. Nevertheless, the high number of parameters defining the optimal configuration of the embedded microchannels topology, thermal loading, etc., make the numerical design of such materials quite challenging.

The focus of the present study is on the computational design of an actively-cooled microvascular fin. The circulation of a coolant in microchannels reduces the temperature of the surrounding

material in two specific ways: (i) by direct extraction of heat from the thermally loaded material, and (ii) by redistributing the heat between hotter and colder regions of the domain. The first mechanism is effective if the length of the embedded microchannels between the inlet and outlet is rather short, i.e., when the fluid exits before it becomes too hot and loses its cooling capacity. MEMS with an active cooling substrate is an example of this type of microvascular materials [12,10]. For microvascular materials with larger dimensions and consequently larger distances between the inlet and outlet of the channels, removing the heat from the domain through active cooling may not effectively reduce the temperature of the domain. In this case, the extracted thermal energy through the fluid only accounts for a small portion of the thermal energy given to the system. Instead, the microvascular network must be designed to effectively redistribute the heat inside the material by extracting the heat from warmer areas of the domain and releasing it in colder regions. An example of nature's designs for this type of actively-cooled systems is the arrangement of blood vessels for the thermal regulation in human skin [13,14]. Depending on environmental conditions, the vascular response of the skin is able to adjust its temperature to preserve or dissipate the heat when the outside temperature is decreased or increased, respectively (Fig. 1(a)).

Additional motivation for the work presented hereafter stems from recent advances in the manufacturing of large, microvascular 3D woven composites based on a novel approach with sacrificial

\* Corresponding author at: Beckman Institute for Advanced Science and Technology, University of Illinois at Urbana-Champaign, 405 North Mathews Avenue, Urbana, IL 61801, USA. Tel.: +1 217 244 7648; fax: +1 217 244 0720.

E-mail address: [geubelle@illinois.edu](mailto:geubelle@illinois.edu) (P.H. Geubelle).

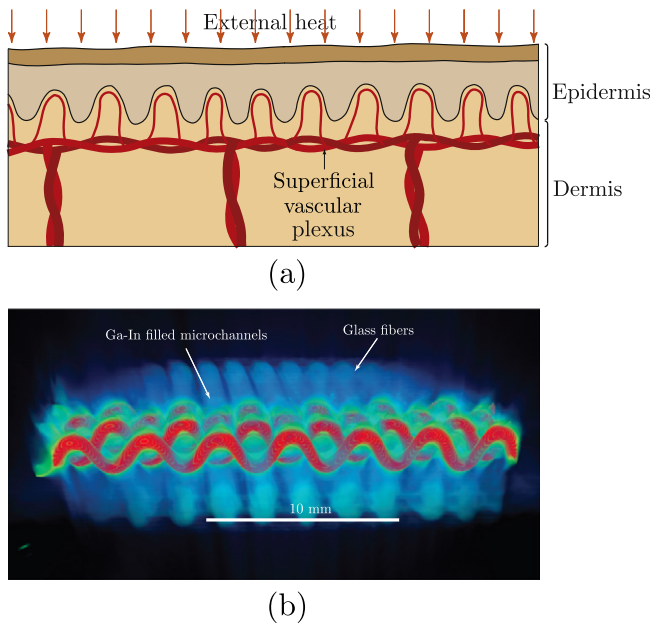


**Fig. 1.** Biological and biomimetic examples of microvascular systems for active cooling: (a) microvascular blood vessels for thermal regulation in the human skin (inspired from [13]); (b) micro-CT image of sinusoidal-shaped microchannels (filled with eutectic Ga–In alloy for a higher resolution) embedded in a 3D woven glass fiber/epoxy matrix composite created with the sacrificial fiber manufacturing technique.

fibers [5]. This method allows for the creation of 3D glass fiber/epoxy matrix composites with sinusoidal microchannels fully integrated into the material microstructure (Fig. 1(b)).

Inspired by these two examples, we adopt a sinusoidal shape for the embedded microchannel in the design study of a microvascular actively-cooled fin, and aim to determine the optimal values of the amplitude and wavelength of the microchannel. While the main objective is to evaluate the optimal geometry of the microchannels to minimize the maximum temperature of the domain, their impact on mechanical properties such as the stiffness of the microvascular material is also addressed indirectly by minimizing the void volume fraction associated with the embedded network. The third objective function adopted in the design study is the minimization of the pressure drop needed to circulate the coolant, i.e., the flow efficiency of the microchannels. Similar optimization problems for the design of microvascular materials have been addressed in [2,15–19].

Although the geometrical setting of the 2D shape optimization study is relatively simple, the efficiency and accuracy of the finite element solver used to predict the impact of the sinusoidal microchannel on the thermal response of the microvascular fin is a critical aspect of this study. Employing the standard finite element method (FEM) for such problems is quite cumbersome since this method requires for each configuration the creation of a mesh that conforms to the microstructure of the material to capture the discontinuity in the gradient field along the fluid/solid interface. Instead, we adopt in this paper a recently introduced generalized finite element method [20,21] to evaluate the temperature field in the microvascular fin. As in conventional Generalized Finite Element Methods (GFEM) [22–24], a priori knowledge of the solution field in the form of weakly discontinuous enrichment functions is incorporated in the numerical approximation of the thermal field. However, instead of introducing nodal enrichment degrees of freedom as in conventional GFEM, the interface-based GFEM formulation (referred to hereafter as IGFEM) applies enrichments at the nodes created by the intersection of the interface with edges of the non-conforming element.

The outline of the paper is as follows: In Section 2, we first present the strong and weak forms of the governing equations describing the temperature field in the actively cooled microvascular material of interest. We then introduce the IGFEM formulation for this problem and briefly discuss some of the key characteristics of the numerical scheme. In Section 3, we summarize the results of a validation study for the IGFEM solver, based on direct comparisons with experimental observations of the thermal field in a microvascular epoxy fin. Finally, we perform in Section 4 a shape optimization study for a sinusoidal microchannel embedded in a long polymeric fin subjected to a uniform heat flux along one of its faces, and investigate how the predicted optimal shape of the microchannel is affected by the choice of thermal boundary conditions.

## 2. Governing equations and IGFEM formulation

To model the temperature field in an actively-cooled microvascular material, we solve the convection–diffusion equations on a 2D domain  $\Omega \subset \mathbb{R}^2$  composed of two mutually exclusive regions  $\Omega_f$  and  $\Omega_s$ , corresponding to the fluid and solid phases in a microvascular material, respectively (Fig. 2). The boundary  $\Gamma = \overline{\Omega} - \Omega$ , with outward unit normal vector  $\mathbf{n}$ , is divided into three mutually exclusive partitions  $\Gamma_T$ ,  $\Gamma_q$ , and  $\Gamma_h$  for assigning the Dirichlet, Neumann, and Robin boundary conditions, respectively. The strong form of the convection–diffusion equation for the open domain  $\Omega$  with the boundary  $\Gamma$  is then expressed as follows: For the given thermal conductivity  $\boldsymbol{\kappa} : \overline{\Omega} \rightarrow \mathbb{R}^2 \times \mathbb{R}^2$ , fluid density  $\rho : \Omega_f \rightarrow \mathbb{R}$ , and specific heat  $c_p : \Omega_f \rightarrow \mathbb{R}$  and the given velocity field  $\mathbf{v} : \Omega_f \rightarrow \mathbb{R}^2$ , find the temperature field  $T : \overline{\Omega} \rightarrow \mathbb{R}$  such that

$$\begin{aligned} -\nabla \cdot (\boldsymbol{\kappa} \nabla T) &= f \quad \text{in } \Omega_s \\ -\nabla \cdot (\boldsymbol{\kappa} \nabla T) + \rho c_p \mathbf{v} \cdot \nabla T &= f \quad \text{in } \Omega_f \\ T &= \bar{T} \quad \text{on } \Gamma_T \\ \boldsymbol{\kappa} \nabla T \cdot \mathbf{n} &= q \quad \text{on } \Gamma_q \\ \boldsymbol{\kappa} \nabla T \cdot \mathbf{n} &= h(T_\infty - T) \quad \text{on } \Gamma_h, \end{aligned} \quad (1)$$

where  $f : \Omega \rightarrow \mathbb{R}$  denotes the heat source,  $\bar{T} : \Gamma_T \rightarrow \mathbb{R}$  the prescribed temperature along the Dirichlet boundary, and  $q : \Gamma_q \rightarrow \mathbb{R}$  the applied heat flux along the Neumann boundary, while  $h : \Gamma_h \rightarrow \mathbb{R}$  and  $T_\infty : \Gamma_h \rightarrow \mathbb{R}$  describe the heat transfer coefficient and ambient temperature along the convective boundary, respectively.

Since this class of problems is characterized by low Reynolds numbers and very narrow channels, the velocity field  $\mathbf{v}$  in the microchannels is adequately described by a fully-developed velocity profile [25]

$$v(r) = 1.5 \frac{\dot{m}}{\rho A} \left(1 - \frac{2r}{D}\right)^2, \quad (2)$$

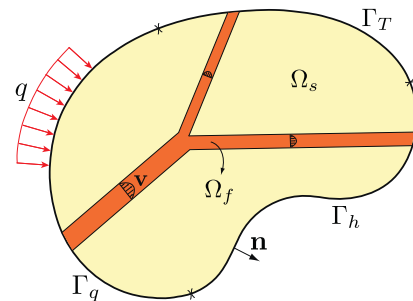


**Fig. 2.** Schematic of a 2D domain  $\Omega = \Omega_s \cup \Omega_f$  with the fluid ( $\Omega_f$ ) and solid ( $\Omega_s$ ) phases. The boundary  $\Gamma$  with outward unit normal  $\mathbf{n}$  is divided into regions  $\Gamma_T$ ,  $\Gamma_q$ , and  $\Gamma_h$  for assigning the Dirichlet, Neumann, and Robin boundary conditions, respectively.

where  $\dot{m}$ ,  $A$ , and  $D$  are the mass flow rate, cross-sectional area, and the diameter of the microchannel, respectively, and  $r$  denotes the distance from the centerline of the microchannel. This assumption therefore neglects the transition distance needed to establish the fully-developed flow conditions as the coolant enters the microchannels, and the impact of possible recirculation that might take place in microchannels with higher curvatures [26,27].

To derive the weak form of (1), we first define  $\mathcal{T} = \{T \in H^1(\bar{\Omega}) : T|_{\Gamma_T} = \bar{T}\}$  and  $\mathcal{W} = \{w \in H^1(\bar{\Omega}) : w|_{\Gamma_T} = 0\}$  as the solution and weight function spaces, respectively. The weak form is then written as: Find  $T \in \mathcal{T}$  such that

$$a(T, w) + a(T, w)_{\Gamma_h} = (w, f) + (w, q)_{\Gamma_q} + (w, T_\infty)_{\Gamma_h} \quad \forall w \in \mathcal{W}, \quad (3)$$

where the linear and bilinear forms in (3) are given by

$$a(T, w) = \int_{\Omega} \nabla w \cdot \boldsymbol{\kappa} \nabla T d\Omega + \int_{\Omega_f} w \rho c_p \mathbf{v} \cdot \nabla T d\Omega, \quad (4)$$

$$a(T, w)_{\Gamma_h} = \int_{\Gamma_h} h w T d\Gamma, \quad (5)$$

$$(w, T_\infty)_{\Gamma_h} = \int_{\Gamma_h} h w T_\infty d\Gamma, \quad (6)$$

$$(w, q)_{\Gamma_q} = \int_{\Gamma_q} w q d\Gamma, \quad (7)$$

$$(w, f) = \int_{\Omega} w f d\Omega. \quad (8)$$

The standard Galerkin FEM formulation for (3) is obtained by the discretization of  $\Omega$  into  $m$  finite elements,  $\Omega \cong \Omega^h \equiv \cup_{i=1}^m \bar{\Omega}_i$  and employing a set of  $n$  Lagrangian shape functions  $\{N_i(\mathbf{x})\}_1^n \subset \mathcal{T}^h$  to approximate the solution field in each element. Using  $\{N_i(\mathbf{x})\}_1^n$  as the weight functions, the standard FEM formulation is then expressed as: Find  $T^h \in \mathcal{T}^h$  such that

$$a(T^h, w^h) + a(T^h, w^h)_{\Gamma_h} = (w^h, f) - a(w^h, \bar{T}^h) + (w^h, q)_{\Gamma_q} + (w^h, T_\infty)_{\Gamma_h} \quad \forall w^h \in \mathcal{W}^h, \quad (9)$$

where

$$T^h(\mathbf{x}) = \sum_{i=1}^n N_i(\mathbf{x}) T_i. \quad (10)$$

As discussed in Section 1, an accurate standard FEM solution for a conjugate heat transfer problem requires the use of meshes that conform to the microchannels. To remove this cumbersome limitation, we adopt in the present study an IGFEM thermal solver, which, like other GFEM formulations, eliminates the need of using conforming meshes by using appropriate enrichment functions to approximate the solution field. The unique feature of the IGFEM, however, is how enrichment functions are evaluated inside the elements cut by the phase interface and how the generalized degrees of freedom (dofs) are assigned. The IGFEM approximation of the solution field in each element is written as [20]

$$T^h(\mathbf{x}) = \sum_{i=1}^n N_i(\mathbf{x}) T_i + \sum_{i=1}^{n_{en}} s \psi_i(\mathbf{x}) \alpha_i. \quad (11)$$

The first term in (11) is the standard FEM part of the approximation with  $T_i$  representing the nodal values of the temperature. The second term is the contribution of enrichment functions in order to capture the gradient discontinuity along the phase interface, where the function space  $\{\psi_i(\mathbf{x}) : \mathbf{x} \rightarrow \mathbb{R}\}_{i=1}^{n_{en}}$  is composed of a set of  $n_{en}$  enrichment functions,  $\alpha_i$  the generalized dofs, and  $s$  is a scaling factor to avoid sharp gradients in the enrichment functions. Unlike conventional GFEM, where the generalized dofs are assigned at the nodes of the original mesh, the IGFEM enrichments are attached

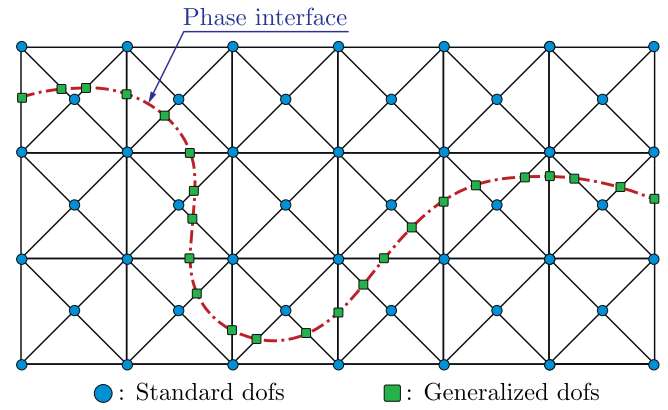


Fig. 3. Location of standard dofs and generalized dofs at the interface nodes in the IGFEM analysis of a domain composed of two phases with the interface shown by a dashed-dotted curve.

to the interface nodes created at the intersection points of elements' edges and the phase interface. Fig. 3 illustrates the location of generalized dofs in the IGFEM at the interface nodes in a domain composed of two phases and discretized with three-node triangular elements.

A key advantage of moving generalized dofs from the nodes of original mesh (as in conventional GFEM) to the interface nodes (as in the IGFEM) appears when assigning Dirichlet boundary conditions at the nodes of elements cut by the interface. Since the standard dofs in the IGFEM directly yield the nodal values of the solution field, applying the prescribed values of the temperature at these nodes is similar to that of the standard FEM. This feature of the IGFEM removes the need of techniques such as the penalty method or Lagrange multipliers to assign Dirichlet boundary conditions at enriched nodes in conventional GFEM formulations [28,29].

The enrichment functions in IGFEM are evaluated as a linear combination of Lagrangian shape functions of the integration elements, i.e., elements created for the Gauss quadrature of the parent element. Fig. 4(a) and (b) illustrate two possible orientations of a three-node triangular element with respect to the phase interface and the corresponding integration elements, which are given by

$$\begin{aligned} (a) \quad & \psi_1 = N_1^{(1)} + N_2^{(2)}, \quad \psi_2 = N_2^{(1)} + N_1^{(2)}, \\ (b) \quad & \psi_1 = N_1^{(1)} + N_1^{(2)}. \end{aligned} \quad (12)$$

To avoid numerical problems caused by the enrichment functions of elements divided into integration elements with high aspect ratios, we use the scaling factor  $s$  in (11) to control the gradient of enrichment functions. The problem arises when an interface node is located too close to one of the nodes of the parent element, causing enrichment functions with very large gradients and possibly leading to ill-conditioned stiffness matrices. To resolve this problem, the enrichment functions are scaled by the factor  $s$  introduced in (11) and defined by  $s = \left(\frac{2 \min(L_1, L_2)}{L_1 + L_2}\right)^2$ , where  $L_1$  and  $L_2$  are the distances between the interface node and the nodes of the parent element's edge (Fig. 5). More information about the IGFEM, including the convergence study and applications, can be found in [20,21].

### 3. Validation study

#### 3.1. Experimental set-up

The schematic and boundary conditions of the microvascular fin used for the validation of the numerical solver are illustrated in Fig. 6. The epoxy matrix, with thermal conductivity  $\kappa_e = 0.23 \text{ W}$

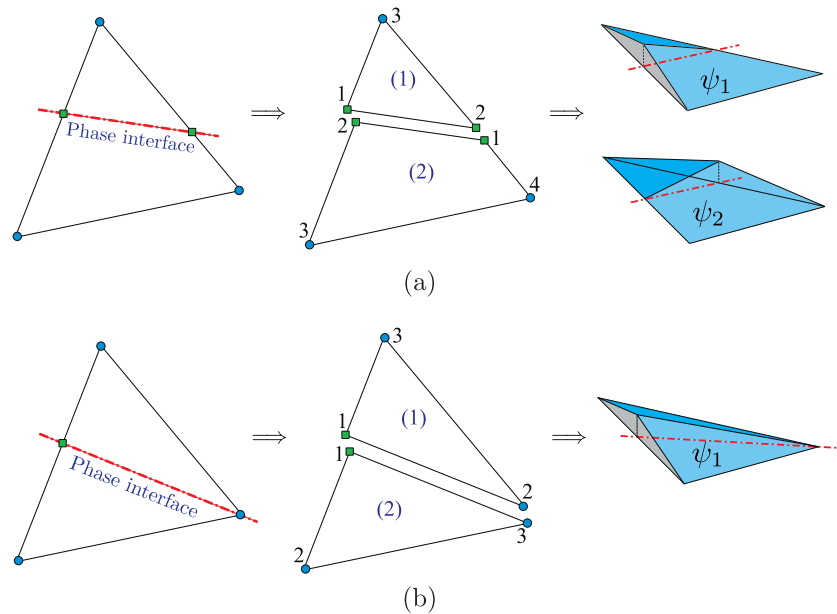


**Fig. 4.** Evaluating the enrichment functions in the IGFEM. Figs. (a) and (b) illustrate two scenarios for creating integration elements and the associated generalized dofs for three-node triangular elements based on the location of the phase interface.

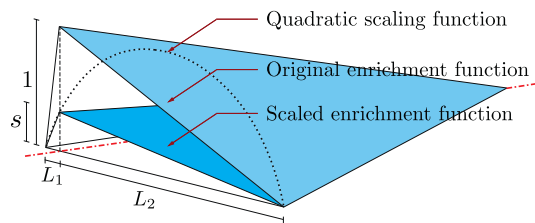


**Fig. 5.** Scaling of the enrichment function for cases where the interface is very close to a node of the underlying non-conforming mesh.

m K, has in-plane dimensions of  $59.4 \times 10.5$  mm and a thickness of 4.0 mm. The microvascular fin is placed on a  $60.0 \times 10.0 \times 0.7$  mm copper plate ( $\kappa_c = 401$  W/m K), which is in contact with a heater supplied with constant power  $P = 2.1$  W. Other faces of the specimen are in contact with air and assumed to have convective boundary conditions with the ambient temperature  $T_\infty = 21$  °C, and a heat transfer coefficient  $h$ , to be determined according to the experimental results obtained in the absence of the flow (Section 3.2). The provided power for the heater and hence the given energy to the copper plate is set such that the temperature along the bottom edge of the domain in the absence of the coolant flow is 80 °C.

The embedded sinusoidal-shaped microchannel in the epoxy fin with diameter  $D = 500$   $\mu\text{m}$ , amplitude  $A = 4$  mm, and wavelength  $\lambda = 10$  mm, is depicted in Fig. 6(a). The distance between the centerline of the microchannel and the surface over which the temperature field is recorded by an infrared camera is about 700  $\mu\text{m}$ . The coolant flowing in the microchannels is water with  $\kappa_w = 0.6$  W/m K,  $\rho = 1000$  kg/m<sup>3</sup>, and  $c_p = 4183$  J/kg K, and the flow rate is maintained constant at  $Q = 2$  ml/min. The test specimen was created with a fugitive organic ink using the direct write assembling [6,30] as shown in Fig. 6(c). The process involves casting a thin epoxy substrate upon which a fugitive ink is robotically deposited in a sinusoidal pattern forming a microchannel template. The pattern is then embedded in epoxy and the entire sample is cured at 50 °C. Removal of the fugitive ink at elevated temperature of 80 °C reveals the embedded microchannel following the pattern

that was formed during deposition. The epoxy used is Epon 862 and Epikure 3300 mixed at 100:24.8 pbw. The fugitive ink used is a mixture of 53% microcrystalline wax (SP-19, Strahl and Pitsch, Inc.) and 47% mineral oil (Fisher Scientific). The ink was extruded from a 500  $\mu\text{m}$  micronozzle at 300 psi at a printing speed of 5 mm/s. The cured specimen was cut and polished to the desired dimensions as shown in Fig. 6(c). One side of the specimen was painted matte black (Krylon) for imaging with an infrared camera. Propylene manifolds were attached to the inlet and outlet opening using cyanoacrylate glue to allow access points for circulation of the coolant through the microchannel.

Active cooling measurements were accomplished using infrared imaging of the microvascular epoxy specimen. The bottom face of the epoxy fin was placed on a copper plate subjected to a constant power boundary condition resulting in a constant starting temperature in the absence of the flow in the microchannel. A thin layer of thermally conductive grease (OmegaTherm) was applied to the bottom face of the composite to improve thermal contact between the copper plate and the fin. A resistive heater (Watlow, 120 V, 15 W) was attached to the copper plate and controlled with a variac controller (STACO Inc., 120 V). A feedback control thermocouple was placed on the top of the plate to monitor the temperature of the plate throughout the experiment. A multimeter was connected in series with the resistive heater to measure the applied voltage. The specimen was allowed to reach steady state by waiting for an hour after application of constant power to the copper plate. Fig. 6(b) shows a schematic of the IR imaging set-up for thermal management.

Infrared images were taken using a DeltaTherm 1560 infrared camera with 320 by 256 array of indium antimonide IR detectors. Data was recorded at one frame per second using DeltaVision software. Each data set contained a 2D temperature field of the specimen surface. The surface temperatures in the absence of flow and steady-state at 2 ml/min are depicted in Fig. 7(a) and (b), respectively. The temperature profiles along lines corresponding to the peak (A) and trough (B) of the sinusoidal microchannel were used for the calibration and validation of the 2D IGFEM model. Water was used as the coolant and was introduced into the sample at room temperature (21 °C) at constant flow rate of 2 ml/min

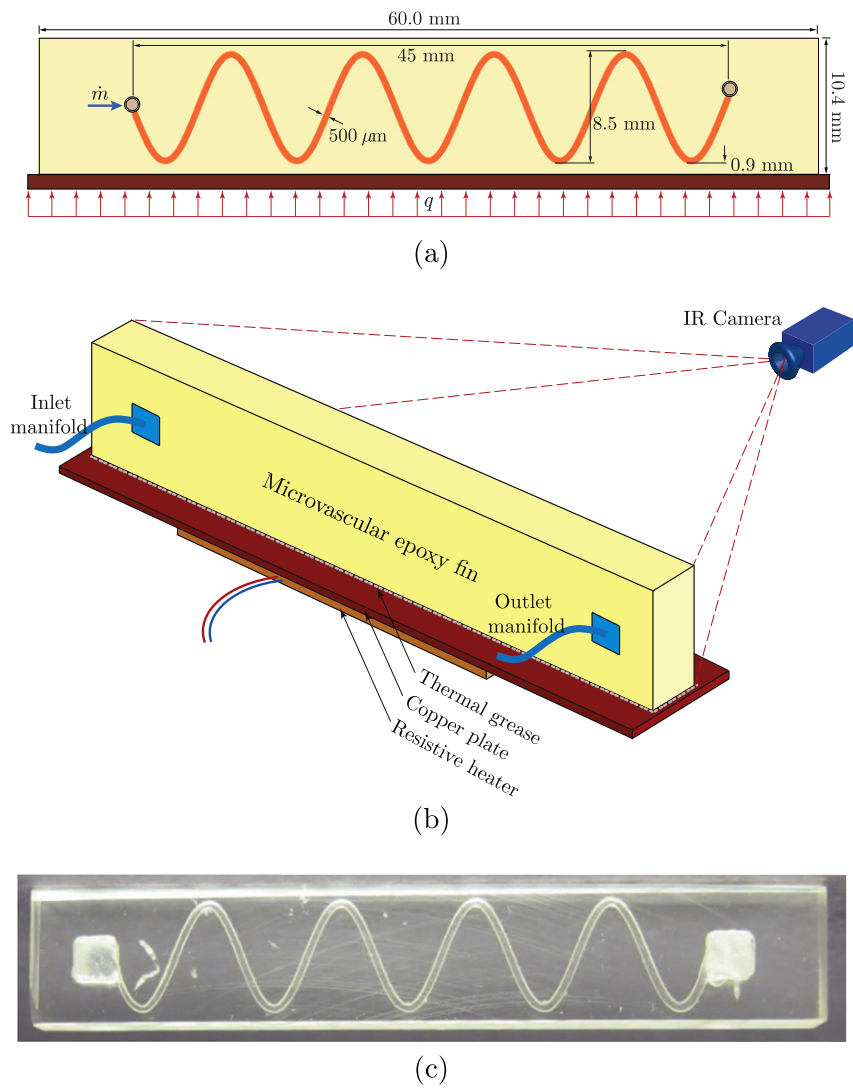


**Fig. 6.** (a) Geometry and boundary conditions of the validation study performed on a thermally loaded microvascular epoxy fin with a 500  $\mu\text{m}$  diameter sinusoidal embedded microchannel; (b) schematic of the experimental set-up with infrared imaging of the temperature field on the surface of the fin; (c) microvascular epoxy fin specimen with embedded microvascular channel created by the direct ink writing technique.

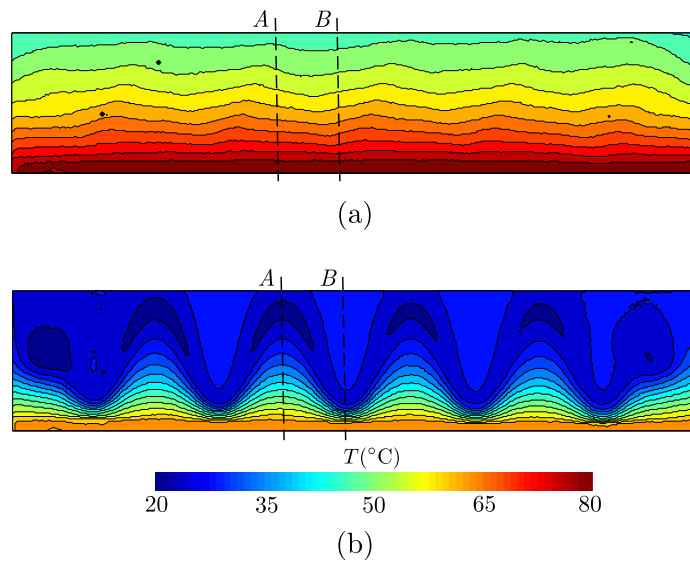


**Fig. 7.** IR image of the steady-state temperature field on the surface of the fin specimen: (a) no flow case; (b) water cooling at 2 ml/min.

maintained using screw driven syringe pump (KD scientific, Model 210).

### 3.2. Calibration and validation of the IGFEM thermal solver

The calibration component of this study consists in evaluating the heat transfer coefficient  $h$ , associated with the surfaces of the specimen in contact with air, which is needed to determine the dissipated heat from these surfaces. To that effect, we use the data obtained with IR measurements in the absence of the flow, as shown in Fig. 7(a). Since a 2D model is adopted for approximating the temperature field, we incorporate the dissipated heat from the faces of the specimen perpendicular to the computational domain by adopting the classical fin equation expressed as

$$-\nabla \cdot (\mathbf{\kappa} \nabla T) = f - \frac{hP}{A}(T - T_\infty), \quad (13)$$

where  $P$  and  $A$  are the perimeter and area of the face of the specimen in contact with the copper plate, respectively.

In the absence of the flow, the temperature field is quasi 1D as apparent both experimentally (Fig. 7(a)) and numerically (Fig. 8(a)). The temperature variation in the fin along a line perpendicular to the copper plate can be analytically expressed as

$$\frac{T - T_\infty}{\bar{T} - T_\infty} = \frac{\cosh \beta(L - y) + \frac{h}{\kappa\beta} \sinh \beta(L - y)}{\cosh \beta L + \frac{h}{\kappa\beta} \sinh \beta L}, \quad (14)$$

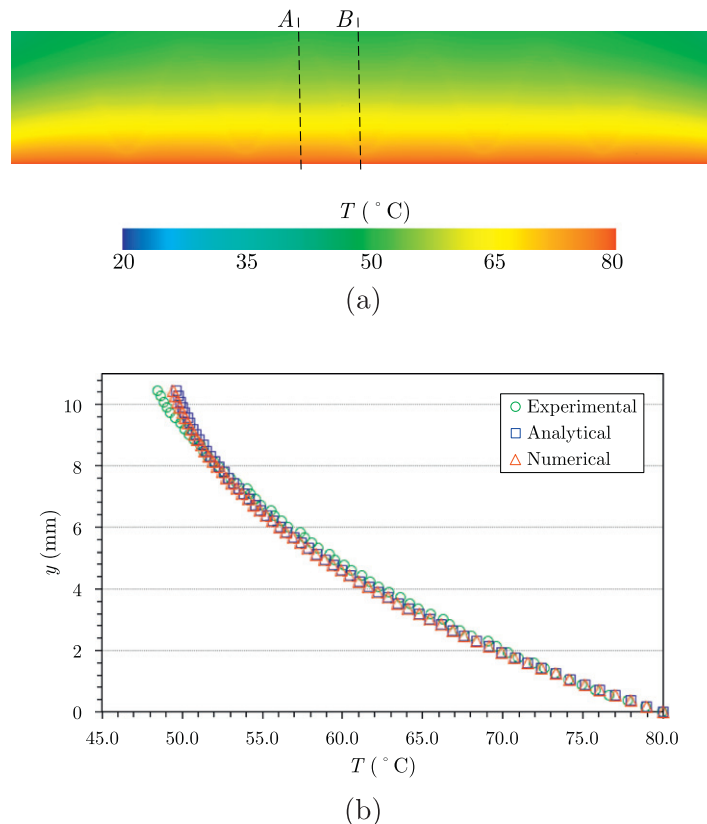
where  $\beta = \sqrt{h_f}$ , with  $h_f = \frac{hP}{\kappa A}$  denoting the fin coefficient. The boundary conditions consist in a prescribed temperature  $\bar{T} = 80^\circ\text{C}$  along the bottom edge of the domain and convective boundary conditions along the top edge. A direct comparison between this relation and the experimental results obtained along line segment A in

Fig. 7(a) yields a least square fit value of the film coefficient  $h$  equal to  $4.9 \text{ W/m}^2\text{K}$ . A comparison between analytical, numerical, and experimental results is presented in Fig. 8(b), showing excellent agreement.

The next step is to evaluate the equivalent flow rate for the 2D solver that yields a similar temperature field as that obtained experimentally. The experimental results for the temperature field after steady state are shown in Fig. 7(b). In this case, the copper plate average temperature is reduced to  $65^\circ\text{C}$  and due to the high thermal conductivity of the copper, this temperature is almost constant at every point along the length of the plate. The equivalent flow rate for the 2D model is then evaluated such that it yields the least square fit of the temperature profiles from the experimental and numerical results along Sections A and B, shown in Fig. 7(b). This calculation gives  $Q_{eq} = 0.724 \text{ ml/min}$ , for which the steady state temperature field obtained from the IGFEM solution and the temperature profiles along Sections A and B are presented in Fig. 9.

To validate the 2D IGFEM solver, we need to examine the performance of this method for evaluating the temperature field in a microvascular material with similar dimensions and boundary conditions, but with a different configuration of the embedded microchannel as illustrated in Fig. 10(a). The heat transfer and fin coefficients for this specimen, which are functions of the dimensions of the domain, are similar to those of the specimen employed in the calibration study (Fig. 6(c)). For the embedded microchannel shown in Fig. 10(a), the wavelength of the channel is reduced to  $\lambda = 5 \text{ mm}$ , and a flow rate of  $Q = 2 \text{ ml/min}$  is used for active cooling of the material. The recorded temperature field with the IR camera over the surface of the actively-cooled specimen, adjacent to the embedded microchannel, is depicted in Fig. 10(b).

The temperature field evaluated by the 2D IGFEM solver for the validation problem is illustrated in Fig. 11(a), where the equivalent



**Fig. 8.** (a) Temperature field obtained with the 2D IGFEM solver in the absence of the flow; (b) experimental, numerical and analytical temperature profiles along Section A. A heat transfer coefficient of  $h = 4.9 \text{ W/m}^2\text{K}$  is employed to evaluate the analytical and numerical solutions.

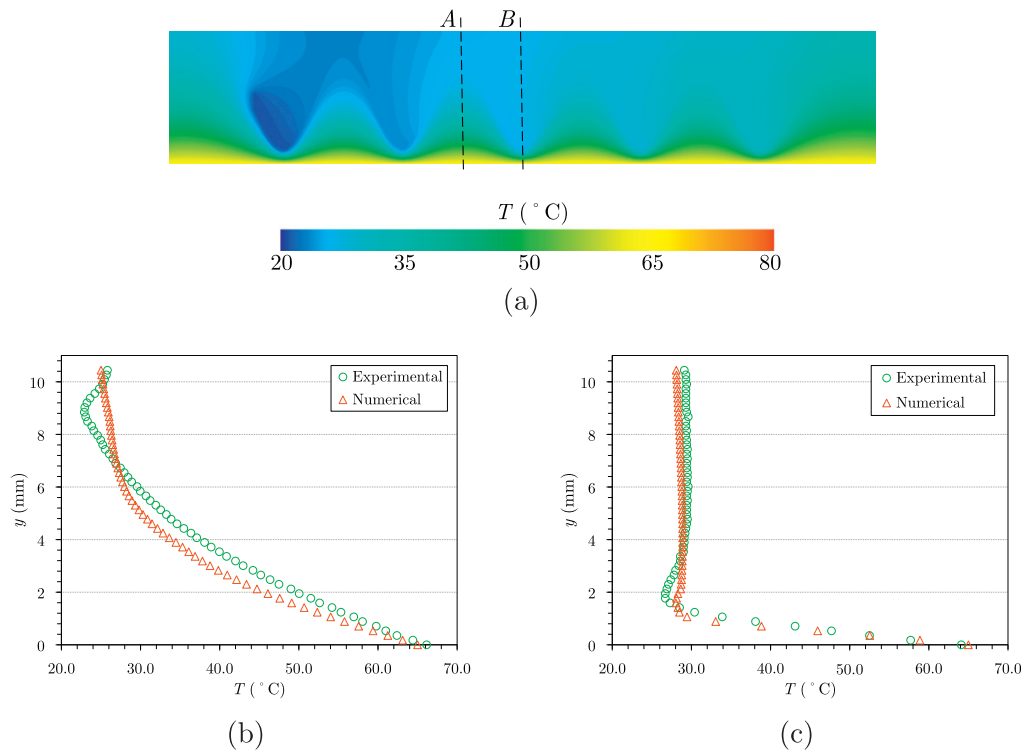


**Fig. 9.** Calibration of the IGFEM solver using the thermally loaded domain with an embedded microchannel with  $\lambda = 10$  mm: (a) steady-state temperature field of the actively-cooled fin at 2 ml/min flow rate obtained with the IGFEM; (b,c) experimental and numerical temperature profiles along Sections A and B, respectively.

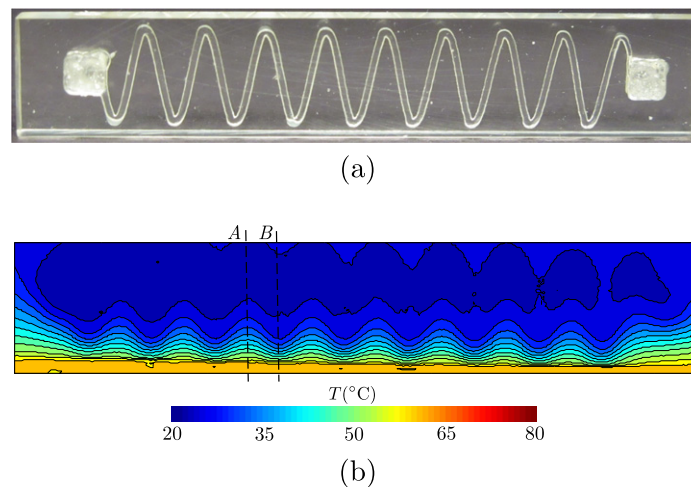


**Fig. 10.** (a) Microvascular fin specimen with an embedded microchannel with wavelength  $\lambda = 5$  mm and amplitude  $A = 4$  mm; (b) IR image of the steady-state temperature field after active cooling at 2 ml/min flow rate.

flow rate obtained from the calibration study ( $Q_{eq} = 0.724$  ml/min) is implemented in the numerical solution. The temperature profiles along Sections A and B (shown in Fig. 10(b)) are presented in Fig. 11(b) and (c), respectively, and compared with experimental values at similar locations. According to this figure, the 2D IGFEM solution has a good agreement with experimental data, especially in predicting the temperature along the top edge of the domain. Considering all the simplifying assumptions implemented in the 2D computational model, this study proves the reliability of the IGFEM in approximating the temperature field in the actively-cooled microvascular fin.

#### 4. Shape optimization of the sinusoidal microchannel

In this section, we aim at determining the optimal configuration of the embedded sinusoidal-shaped microchannel in the epoxy fin shown in Fig. 12. The height and thickness of this domain are similar to those of the microvascular fin specimen depicted in Fig. 6 used for the calibration and validation of the IGFEM thermal solver. The heat transfer and fin coefficients for the shape optimization problem are similar to those obtained in the previous section. The length of the microvascular fin, however, has been increased to 180 mm to investigate the effect of the specimen length on the

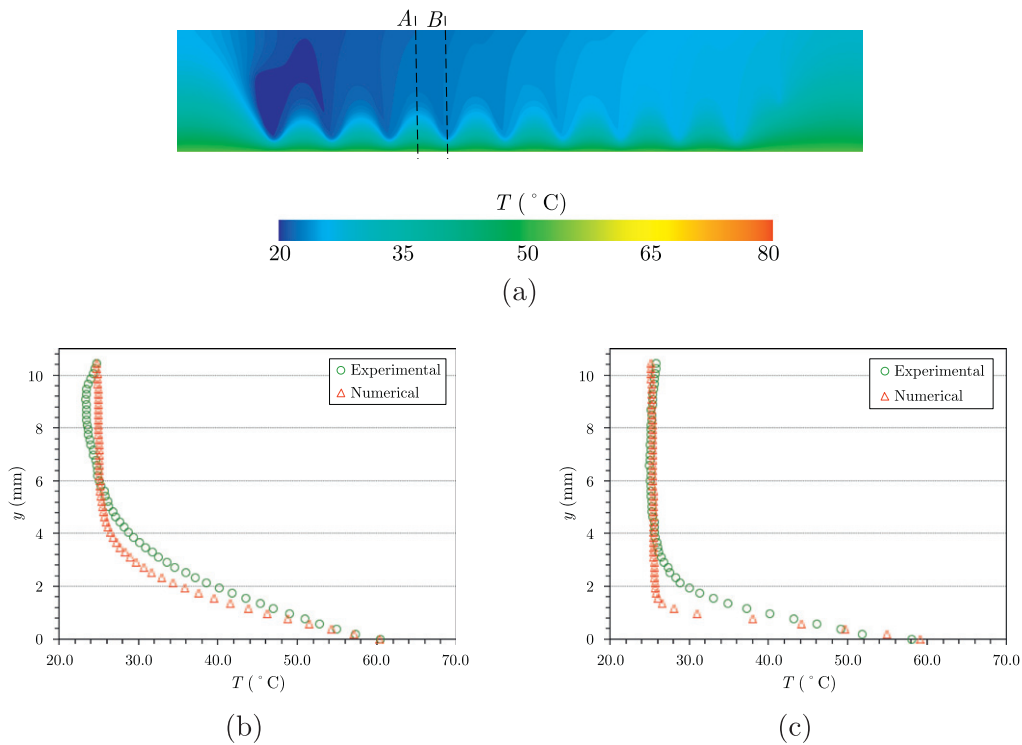


**Fig. 11.** Validation of the IGFEM solver based on the microvascular fin with  $\lambda = 5$  mm: (a) steady-state temperature field of the actively-cooled fin at 2 ml/min flow rate obtained with the IGFEM; (b,c) experimental and numerical temperature profiles along Sections A and B, respectively.

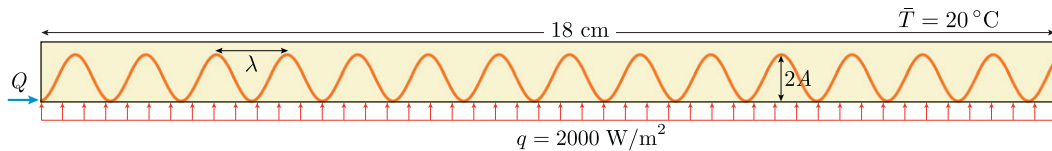


**Fig. 12.** Schematic and boundary conditions of the microvascular fin investigated in the shape optimization study.

optimal shape of the embedded microchannel. The thermal boundary conditions consist of a convective boundary condition along the left and right sides of the 2D computational domain and constant heat flux  $q = 2000 \text{ W/m}^2$  along the bottom edge. Two different conditions are considered along the top edge to study their impact on the predicted optimal configuration of the embedded microchannel: (i) a fixed temperature of  $\bar{T} = 20^\circ\text{C}$  and (ii) a convective boundary condition with  $h = 4.9 \text{ W/mK}$  and  $T = 21^\circ\text{C}$ .

The optimization problem aims at determining the optimal amplitude,  $A$ , and wavelength,  $\lambda$ , of the sinusoidal microchannel that minimizes a set of three objective functions  $\Phi = \{\phi_i\}_{i=1}^3$ : (i) the maximum temperature of the polymer matrix, (ii) its void volume fraction, and (iii) the pressure drop. Details on the evaluation of these three objective functions are provided below. The entrance of the microchannel is at the left edge and the minimum distance between its centerline and the bottom edge of the domain is  $580 \mu\text{m}$  for all configurations. Similar to the previous section, water is employed as the coolant with  $Q = 1 \text{ ml/min}$ , which, based on the study presented in the previous section, corresponds to an equivalent flow rate of  $Q_{eq} = 0.362 \text{ ml/min}$  for the 2D model.

The minimum and maximum values of the wavelength  $\lambda$  are set to 7.5 and 30 mm, respectively, with increments of 2.5 mm while the minimum and maximum values of  $A$  are 0 and 4.8 mm, respectively, with increments of  $400 \mu\text{m}$ . The aforementioned parameters provides a total number of 121 different configurations for which the small size of the search space allows for analyzing and evaluating the objective functions for all possible cases. This is

specifically possible by using the IGFEM solver, for which a single non-conforming structured mesh built on a  $1080 \times 63$  grid is employed to evaluate the temperature field associated with all the microchannel configurations. The objective functions considered in this optimization problem are as follows:

**Maximum temperature:** Reducing the maximum temperature of the domain is the main goal of designing actively-cooled microvascular systems. We thus define the first objective function as

$$\phi_1 = T_{max} : \Omega^h \rightarrow \mathbb{R} := \max T^h, \quad (15)$$

where  $T^h$  is obtained from (9) using the IGFEM solver. For this particular optimization problem, the maximum temperature is typically obtained along the lower edge of the specimen, along which the heat flux is applied.

**Void volume fraction:** While reducing the maximum temperature of the domain constitutes the primary objective, a successful design for the microvascular network must be minimally invasive with respect to the mechanical properties of the material, and in particular its strength and stiffness. As a first approximation, the impact of the microchannel on these mechanical properties can be related to the void volume fraction associated with the embedded network. The second objective function thus consists in minimizing

$$\phi_2 = V_f \in R := \frac{\int_{\Omega^h} \pi D^2 ds}{4V_{\Omega^h}}, \quad (16)$$

where  $V_{ch}$  is the total volume of the microvascular material,  $L_f$  and  $D$  are respectively the length and diameter of the channel, and  $ds$  is a longitudinal element at the centerline of the microchannel. It must be noted that, due to the constant diameter of the microchannels, minimizing this objective function corresponds to minimizing the length of the embedded microchannel for the current system.

**Pressure drop:** The third objective function is defined as the required pressure to move the coolant between the inlet and the outlet of the microchannel:

$$\phi_3 = \Delta p \in \mathbb{R} := \max |p_{in} - p_{out}|. \quad (17)$$

This pressure drop is directly related to the flow efficiency of the microchannel, because the power required to circulate the fluid is expressed as  $P = \dot{m}\Delta p/\rho$ . Assuming a fully-developed flow velocity profile as described by (2), the pressure drop in the microchannel is obtained from the *Hagen-Poiseuille* law [25]

$$\Delta p = \int_{L_f} \frac{128\mu(T_f)\dot{m}ds}{\rho\pi D^4}, \quad (18)$$

where  $\mu$  is the dynamic viscosity of the coolant, which is a decreasing function of its temperature  $T_f$ . In the current study, we use the *Seeton fit* [31] to approximate the temperature dependence of the viscosity for water:

$$\mu(T_f) = C \times 10^{\frac{T_1}{T_f - T_2}}, \quad (19)$$

where  $C = 2.414 \times 10^{-5}$  N s/m<sup>2</sup>,  $T_1 = 247.8$  K, and  $T_2 = 140$  K. The dynamic viscosity of water is then evaluated along each longitudinal cross section  $ds$  of the microchannel according to (19) to determine the pressure drop in that cross section.

#### 4.1. Prescribed temperature along the top edge

Assuming a prescribed temperature of  $T_t = 20$  °C along the upper edge of the domain (Fig. 12), the numerical predictions obtained with the IGFEM thermal solver are presented in Fig. 13. The values of the objective functions for each individual, i.e., each data point corresponding to one of the configurations of the microchannel, are depicted in Fig. 13(a). The void volume fraction versus the maximum temperature of the domain for each individual is shown in Fig. 13(b) to better illustrate the variations of these two objective functions for different configurations. As shown there, the individuals corresponding to the lowest values of the void volume fraction maintain a relatively low maximum temperature in the domain. The maximum temperature of the domain then increases with the void volume fraction until it reaches a peak value beyond which, the microchannels with higher void volume fractions are more effective in reducing the maximum temperature.

The variations of the maximum temperature of the material with respect to the wavelength and the amplitude of the microchannels, and with respect to its amplitude for  $\lambda = 7.5$  mm are shown in Fig. 13(c) and (d), respectively. As shown in Fig. 13(d), a straight microchannel between the inlet and the outlet ( $A = 0$  mm) reduces the maximum temperature of the domain to  $T_{max} = 60.8$  °C. Increasing the amplitude of the microchannel up to  $A = 3.6$  mm not only increases the void volume fraction, but also is less effective in decreasing the maximum temperature of the domain. After this point, however, microchannels with higher amplitudes yield more effective configurations for reducing the maximum temperature compared to the straight channel, although this comes at the price of a higher void volume fraction and pressure drop.

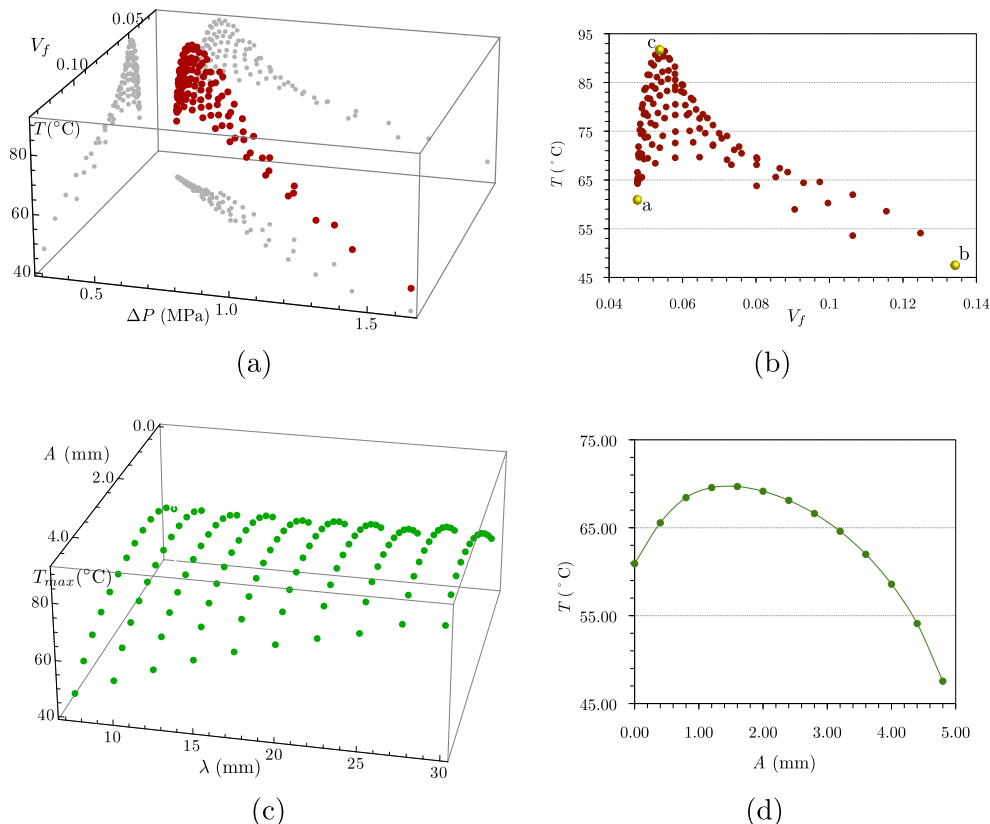


**Fig. 13.** Optimization results for the problem shown in Fig. 12 with a prescribed temperature along the top edge: (a) representation of three and (b) two objective functions for each individual; (c) maximum temperature versus the wavelength  $\lambda$  and microchannel amplitude  $A$ ; (d) maximum temperature in the fin versus the microchannel amplitude for  $\lambda = 7.5$  mm.

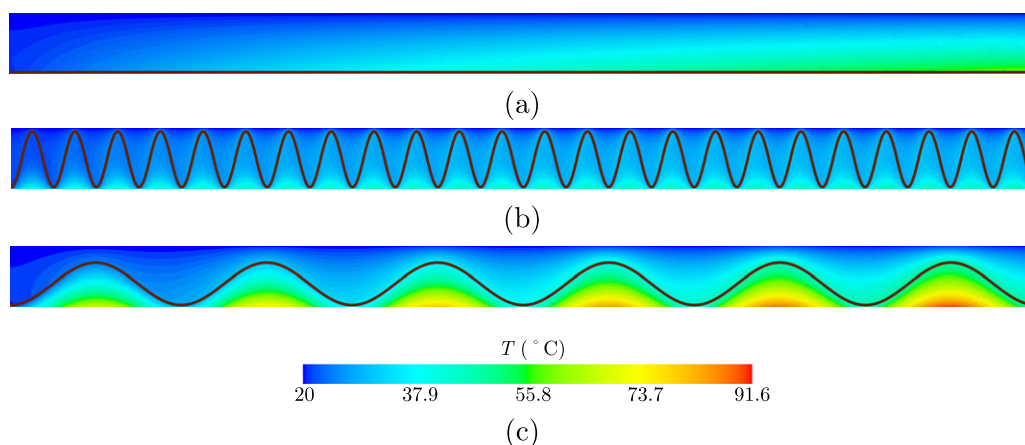


Fig. 14. Temperature field associated with the configuration labeled as (a–c) in Fig. 13(b).

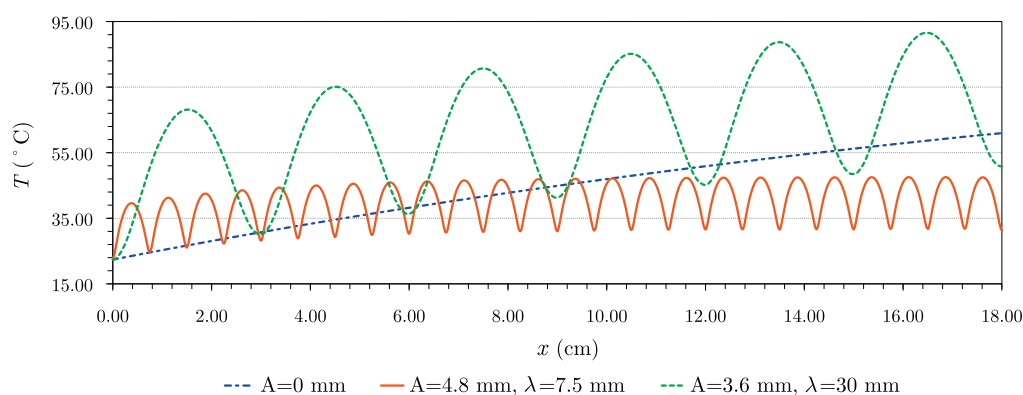


Fig. 15. Temperature profile along the bottom edge of domain associated with the microchannels shown in Fig. 14.

The temperature fields for the individuals marked as (a–c) in Fig. 13(b) are illustrated in Fig. 14(a–c), respectively. As expected, the temperature field associated with the straight microchannel shown in Fig. 14(a) corresponds to the best configuration for minimizing the void volume fraction and pressure drop. The microchannel shown in Fig. 14(b) with the minimum wavelength and maximum amplitude is the most effective for reducing the maximum temperature, although this configuration yields the highest void volume fraction and pressure drop. Finally, the microchannel corresponding to the highest temperature over the domain and the associated temperature field are depicted in Fig. 14(c).

The impact of the microchannel configuration on reducing the maximum temperature of the domain can be better understood by studying Fig. 15. This figure illustrates the temperature profile along the bottom edge of the domain, where the maximum temperature occurs, for the three microchannels shown in Fig. 14. The temperature profile associated with the straight microchannel has a roughly constant rate of increase along this edge. For this microchannel, the only mechanism that contributes to active cooling of the domain is removing the heat through the outgoing flow. Therefore, as we move towards the right edge of the domain, the maximum temperature of the material increases due to the increase of the coolant temperature and hence the reduction of its cooling capacity.

The temperature profile along the bottom edge of the domain associated with the sinusoidal channel depicted in Fig. 14(b) ( $A = 4.8$  mm,  $\lambda = 7.5$  mm) reveals a different thermal response. As shown in Fig. 15, after only a few oscillations of the microchannel,

the temperature along the bottom edge reaches a periodic state where the inflow and outflow temperatures of the fluid at the beginning and the end of each phase are similar. This is achieved through the heat exchange between the lower and upper regions of the domain, i.e., the warmer and colder areas, respectively, such that the amount of the extracted and transmitted heat in each region are equal. As explained in Section 1, configurations that can effectively redistribute the heat inside the domain are better options for active cooling of domains similar to that of the current problem with large distances between the inflow and outflow points. Compared to the straight channel, Fig. 15 verifies that the sinusoidal microchannel with  $A = 4.8$  and  $\lambda = 7.5$  mm is more effective in reducing the maximum temperature of the material if the length of the domain exceeds 10 cm. Moreover, the sinusoidal configuration maintains the same maximum temperature regardless of the length of the domain while the maximum temperature associated with the straight microchannel has an increasing rate with increasing the length of the domain.

The temperature profile associated with the microchannel corresponding to the highest maximum temperature over the domain with  $A = 3.6$  and  $\lambda = 30$  mm shows a similar behavior as the previous case. However, the large wavelength and average amplitude of this channel which do not let effective heat exchange with the cold region near the upper edge of the domain yields a much higher maximum temperature and has not reached the periodic state within the length of the domain. It must be noted that as shown in Fig. 15, the increasing rate of the temperature along the bottom edge associated with this sinusoidal configuration is lower than

that of the straight microchannel. Thus, it is not difficult to predict that as the length of the domain increases, even this configuration will eventually be more effective for active cooling of the domain compared to the straight channel.

4.2. Convective boundary conditions along the top edge

Fig. 16 illustrates the optimization results corresponding to those shown in Fig. 13, but assuming convective boundary conditions along the top edge of the domain. As shown there, the change of boundary conditions has a substantial effect on the optimal configuration of the microchannel, as the straight channel represents the optimal shape with respect to all the objective functions in this case. In other words, increasing either the wavelength or the

amplitude of the microchannels not only exacerbates the void volume fraction and the pressure drop, but also has an adverse impact on the maximum temperature of the material.

The temperature fields and microchannel configurations for the three individuals labeled as (a–c) in Fig. 16(b) are depicted in Fig. 17(a–c), respectively. The corresponding temperature profiles along the bottom edge of the fin are illustrated in Fig. 18. The temperature field associated with the straight channel, depicted in Fig. 17(a), is very similar to that shown in Fig. 14(a) with prescribed temperature along the top edge. Comparing Figs. 18 and 15, we observe that the variations of the temperature along the bottom edge for both cases are almost identical. However, unlike the problem with prescribed temperature along the top edge, the straight microchannel is the best configuration for reducing the maximum temperature of the domain in the current case.

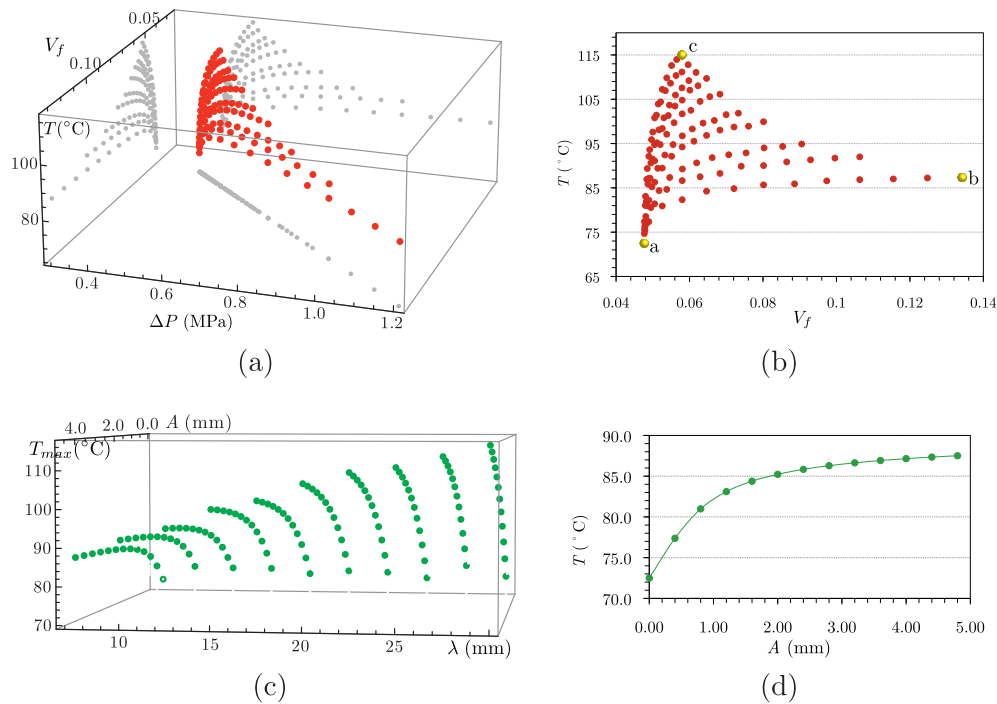


Fig. 16. Optimization results for the problem shown in Fig. 12 with convective boundary conditions along the top edge: (a) representation of three and (b) two objective functions for each individual; (c) maximum temperature versus the wavelength  $\lambda$  and microchannel amplitude  $A$ ; (d) maximum temperature in the fin versus the microchannel amplitude for  $\lambda = 7.5$  mm.

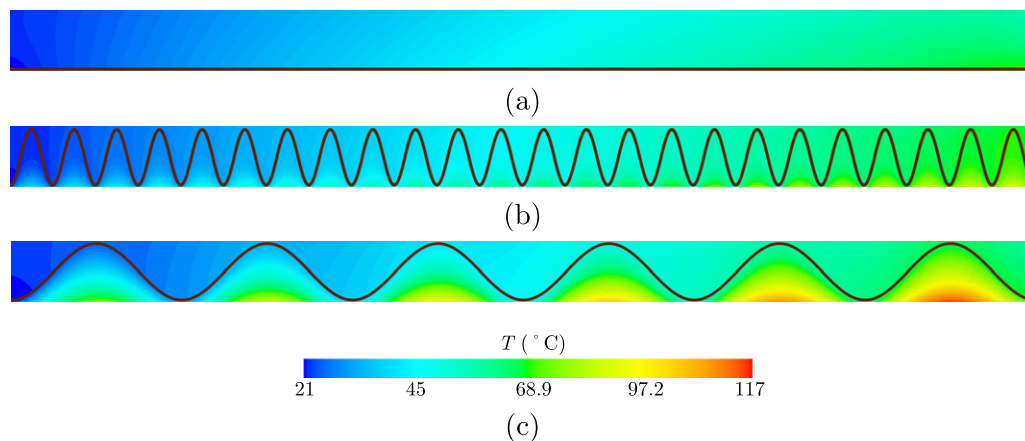


Fig. 17. Temperature field associated with the individuals labeled as (a–c) in Fig. 17(a).

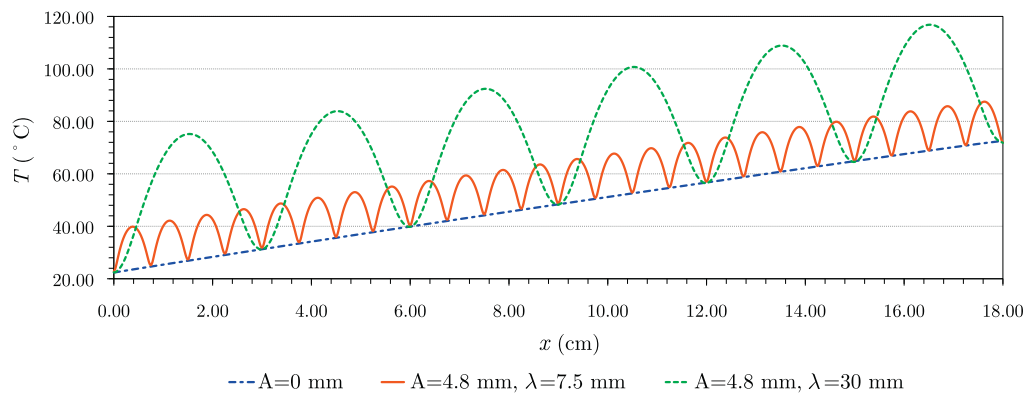


Fig. 18. Temperature profile along the bottom edge of domain associated with the microchannels shown in Fig. 17.

Fig. 17(b) and (c) illustrate the microchannels associated with the highest void volume fraction (and pressure drop) and highest maximum temperature over the domain, respectively. As shown in Fig. 18, despite the sinusoidal shape of the microchannel and thus the heat exchange between the lower and upper edges of the domain, the temperature along the bottom edge never shows a periodic behavior. The reason is that when the coolant flows towards the top edge, it increases the temperature of the matrix in that region and hence the oscillations of the microchannel for exchanging the heat between the top and bottom edges become ineffective for reducing the temperature of the coolant along the length of the domain. This behavior is completely different from the previous case with the prescribed temperature along the top edge, where the rate of increase of the temperature was descending and a periodic state was eventually emerging. Thus, the only efficient configuration for active cooling of the problem shown in Fig. 12 with convective boundary conditions along the top edge is a straight microchannel between the inlet and outlet. However, the straight configuration is only effective along a short length due to the increasing temperature of the coolant, which deteriorates its cooling capacity. For longer domains with similar boundary conditions, multiple inlets and outlets must be considered at appropriate distances along the length of the material to avoid excessive increase of the temperature of the coolant before existing the domain.

## 5. Conclusions

The optimal configuration of the embedded sinusoidal microchannel in an epoxy fin was studied. An interface-enriched GFEM (IGFEM) was employed to evaluate the temperature field for different configurations of the microchannel. This method provides independence between the structure of the finite element mesh and geometry of the problem. Moreover, the IGFEM provides several advantages over conventional GFEM including the easy assignment of Dirichlet boundary conditions at enriched elements and low computational cost. The IGFEM solver was calibrated and validated using the experimental data obtained from thermal tests performed on a microvascular epoxy fin. The heat transfer and fin coefficients of the domain were evaluated using the results of the test in the absence of active cooling, while the data obtained from the actively-cooled fin were employed to extract the equivalent 2D flow rate. The IGFEM model was then validated by evaluating the temperature field in a similar microvascular fin with a different microchannel configuration and comparing that with the experiment. Finally, we employed the IGFEM solver to determine the optimal microchannel configurations by finding the wavelength and amplitude of the sinusoidal channel that minimize the

maximum temperature, void volume fraction, and the pressure drop for circulating the fluid. We also studied the impact of boundary conditions on the optimal configuration of the channels, which proved to be a decisive factor in the design of the microvascular fin.

## Acknowledgment

This work has been supported by the Air Force Office of Scientific Research Multidisciplinary University Research Initiative (Grant No. FA9550-09-1-0686).

## References

- [1] K.S. Toohy, N.R. Sottos, J.A. Lewis, J.S. Moore, S.R. White, Self-healing materials with microvascular networks, *Nat. Mater.* 6 (2007) 581–585.
- [2] A.M. Aragón, J.K. Wayer, P.H. Geubelle, D.E. Goldberg, S.R. White, Design of microvascular flow networks using multi-objective genetic algorithms, *Comput. Methods Appl. Mech. Eng.* 197 (2008) 4399–4410.
- [3] A. Bejan, S. Lorente, K.-M. Wang, Networks of channels for self-healing composite materials, *J. Appl. Phys.* 100 (3) (2006) 033528.
- [4] S.C. Olugebefola, A.M. Aragón, C.J. Hansen, A.R. Hamilton, B.D. Kozola, W. Wu, P.H. Geubelle, J.A. Lewis, N.R. Sottos, S.R. White, Polymer microvascular network composite, *J. Compos. Mater.* 44 (22) (2010).
- [5] A.P. Esser-Kahn, P.R. Thakre, H. Dong, J. Patrick, N.R. Sottos, J.S. Moore, S.R. White, Three dimensional microvascular fiber-reinforced composites, *Adv. Mater.* 23 (32) (2011) 3654–3658.
- [6] D. Theriault, S.R. White, J.A. Lewis, Chaotic mixing in three-dimensional microvascular networks fabricated by direct-write assembly, *Nat. Mater.* 2 (2003) 256–271.
- [7] M.A. Burns, B.N. Johnson, S.N. Brahmasandra, K. Handique, J.R. Webster, M. Krishnan, T.S. Sammarco, P.M. Man, D.JonesD. Heldsinger, C.H. Mastrangelo, D.T. Burke, An integrated nanoliter DNA analysis device, *Science* 282 (1998) 484–487.
- [8] A. Strömberg, A. Karlsson, F. Ryttsén, M. Davidson, D.T. Chiu, O. Orwar, Microfluidic device for combinatorial fusion of liposomes and cells, *Anal. Chem.* 73 (2001) 126–130.
- [9] N.L. Jeon, S.K.W. Dertinger, D.T. Chiu, I.S. Choi, A.D. Strook, G.M. Whitesides, Generation of solution and surface gradients using microfluidic systems, *Langmuir* 16 (2000) 8311–8316.
- [10] V.G. Pastukhov, Y.F. Maidanik, C.V. Vershinin, M.A. Korukov, Miniature loop heat pipes for electronics cooling, *Appl. Therm. Eng.* 23 (9) (2003) 1125–1135.
- [11] X. Wei, Y. Joshi, M.K. Patterson, Experimental and numerical study of a stacked microchannel heat sink for liquid cooling of microelectronic devices, *J. Heat Transfer* 129 (10) (2007) 1432–1444.
- [12] R.B. Oueslati, D. Theriault, S. Martel, PCB-integrated heat exchanger for cooling electronics using microchannels fabricated with the direct-write method, *IEEE Trans. Compon. Pack. Technol.* 31 (4) (2008) 869–874.
- [13] E. Benfeldt, In vivo microdialysis for the investigation of drug levels in the dermis and the effect of barrier perturbation on cutaneous drug penetration, Master's thesis, Department of Dermatology, Gentofte Hospital, University of Copenhagen, Hellerup, Denmark, 1999.
- [14] E. Lehmuskallio, Cold protecting emollients and frostbite, Master's thesis, Department of Dermatology and Venerology, University of Oulu, 2001.
- [15] A.M. Aragón, C. J. W. Wu, P.H. Geubelle, J.A. Lewis, S.R. White, Computational design and optimization of a biomimetic self-healing/cooling material, in: *Proceedings of SPIE*, vol. 6526, 2007.
- [16] A. Bejan, Constructal-theory network of conducting paths for cooling a heat generating volume, *Int. J. Heat Mass Transfer* 40 (4) (1997) 799–816.

- [17] S. Kim, S. Lorente, A. Bejan, Vascularized materials: tree-shaped flow architectures matched canopy to canopy, *J. Appl. Phys.* 100 (2006) 063525–063528.
- [18] H. Zhang, S. Lorente, A. Bejan, Vascularization with trees that alternate with upside-down trees, *J. Appl. Phys.* 101 (9) (2007) 094904.
- [19] A. Bejan, S. Lorente, *Design with constructal theory*, Wiley, Hoboken, 2008.
- [20] S. Soghrati, A.M. Aragón, C.A. Duarte, P.H. Geubelle, An interface-based generalized finite element method for problems with discontinuous gradient fields, *Int. J. Numer. Methods Eng.* 89 (8) (2012) 991–1008.
- [21] S. Soghrati, P.H. Geubelle, A 3D interface-enriched generalized finite element method for weakly discontinuous problems with complex internal geometries, *Comput. Methods Appl. Mech. Eng.* 217–220 (2012) 46–57.
- [22] N. Moës, M. Cloirec, P. Cartraud, J.F. Remacle, A computational approach to handle complex microstructure geometries, *Comput. Methods Appl. Mech. Eng.* 192 (2003) 3163–3177.
- [23] N. Sukumar, Z. Hang, J.H. Prevost, Z. Suo, Partition of unity enrichment for bimaterial interface cracks, *Int. J. Numer. Methods Eng.* 59 (2004) 1075–1102.
- [24] A.M. Aragón, C.A. Duarte, P.H. Geubelle, Generalized finite element enrichment functions generalized finite element enrichment functions for discontinuous gradient fields, *Int. J. Numer. Methods Eng.* 82 (2010) 242–268.
- [25] C.A. Brebbia, A. Ferrante, *Computational Hydraulics*, Butterworth, 1983.
- [26] G. Wang, S.P. Vanka, Convective heat transfer in periodic wavy passages, *Int. J. Heat Mass Transfer* 38 (17) (1995) 3219–3230.
- [27] C.C. Wang, C.K. Chen, Forced convection in a wavy-wall channel, *Int. J. Heat Mass Transfer* 45 (12) (2002) 2587–2595.
- [28] I. Babuska, U. Banerjee, O. JE, Survey of meshless and generalized finite element methods: a unified approach, *Acta Numer.* 12 (2003) 1–125.
- [29] N. Moës, E. Béchet, M. Tourbier, Imposing dirichlet boundary conditions in the extended finite element method, *Int. J. Numer. Methods Eng.* 67 (12) (2006) 1641–1669.
- [30] J. Lewis, Direct writing of 3D functional materials, *Adv. Funct. Mater.* 16 (17) (2006) 2193–2204.
- [31] C.J. Seeton, Viscosity-temperature correlation for liquids, *Tribol. Lett.* 22 (1) (2006).